# What Determines the fcc-bcc Structural Transformation in Shock Compressed Noble Metals?

Surinder M. Sharma,[1] Stefan J. Turneaure,[1] J. M. Winey ,[1] and Y. M. Gupta [1,2,*]

[1]*Institute for Shock Physics, Washington State University, Pullman, Washington 99164, USA*
[2]*Department of Physics and Astronomy, Washington State University, Pullman, Washington 99164, USA*

High pressure structural transformations are typically characterized by the thermodynamic state (pressure-volume-temperature) of the material. We present *in situ* x-ray diffraction measurements on laser-shock compressed silver and platinum to determine the role of deformation-induced lattice defects on high pressure phase transformations in noble metals. Results for shocked Ag show a copious increase in stacking faults (SFs) before transformation to the body-centered-cubic (bcc) structure at 144–158 GPa. In contrast, shock compressed Pt remains largely free of SFs and retains the fcc structure to over 380 GPa. These findings, along with recent results for shock compressed gold, show that SF formation promotes high pressure structural transformations in shocked noble metals that are not observed under static compression. Potential SF-related mechanisms for fcc-bcc transformations are discussed.

Shock wave and static high pressure studies provide a comprehensive approach for understanding condensed matter states at extreme thermodynamic conditions. Under static compression [e.g., diamond anvil cell (DAC) experiments], materials are subjected to nearly isotropic strains (negligible shear strains). In contrast, shock wave compression results in uniaxial strain and concomitant temperature increase. Uniaxial strain compression—beyond the elastic limit— leads to plastic deformation resulting in significant microstructural changes, including generation of lattice defects. Equation of state (EOS) studies and related developments, carried out extensively over several decades, have attempted to reconcile the shock and static compression results at high pressures (∼100 GPa and higher) by treating temperature increase as the primary difference between shock compressed and statically compressed states [1,2]. Unlike temperature, the role of differing strains on the high pressure states achieved under shock and static compression has received minimal attention.

It is commonly accepted that materials adopt unique equilibrium crystal structures for given thermodynamic conditions (pressure, density, and temperature), irrespective of the state of strain. Indeed, the high pressure crystal structures attained under shock compression are considered to have an almost one-to-one correspondence with phases observed under static compression [3–8], despite significant differences in the strain states. This correspondence, in much of the shock compression studies to date, is based primarily on indirect inferences from wave profile measurements or Hugoniot results [3] since direct structure determination, in general, has not been possible; such continuum measurements are also not sensitive to phase transitions having small volume changes [3].

Recent experimental developments using x-ray light sources have resulted in high quality x-ray diffraction (XRD) measurements on shocked solids, providing direct *in situ* determination of crystal structures [5–8] and microstructural changes [9–11] in real time. These developments provide atomistic level comparisons between shock and statically compressed states, addressing a long-standing need in high pressure research.

Face-centered-cubic (fcc) noble metals—due to their structural stability under static compression [12–17] and in Hugoniot measurements [18–22]—are considered ideal pressure markers. However, recent XRD studies on gold have shown that the fcc structure is not stable under shock compression, transforming to the body-centered-cubic (bcc) phase above ∼150 GPa [23,24]. In addition, *in situ* XRD results on shock-compressed gold have established the copious generation of stacking faults (ABCBCA stacking of {111} fcc planes, instead of ABCABC stacking) below the threshold stress for the fcc-bcc transformation [11]; the abundance of stacking faults (SFs) was shown to increase monotonically up to a shock stress of ∼150 GPa, where almost every sixth atomic layer was a SF.

Because the fcc-bcc transformation in gold is neither observed experimentally under static compression nor predicted to occur along the calculated Hugoniot [25], the copious SF production under shock compression raises the following fundamental question: Are the two findings noted above for shock compressed gold linked? That is, do SFs generated during shock compression play a significant role in facilitating fcc-bcc transformations in shocked noble metals?

To address this question, we have investigated two more noble metals: silver, where we expected to observe significant shock-induced stacking faults; and platinum, where we

expected very low abundance of shock-induced stacking faults. Our expectations regarding the abundance of stacking faults in Ag, but not in Pt, were based on the well-known correlation with the stacking fault energy established previously in quasistatic (uniaxial stress) experiments at low stresses [26]. Pt possesses a much higher stacking fault energy (SFE) than Au, whereas Ag has a slightly lower SFE than Au (SFE: Pt $\sim$ 322 mJ/m$^2$, Au $\sim$ 32 mJ/m$^2$, and Ag $\sim$ 16 mJ/m$^2$ [26–28]). Therefore, based on the results for shocked Au [11], SF generation is a more likely deformation mechanism in shocked Ag than in shocked Pt.

Here, we present results from *in situ* XRD measurements on shock compressed silver and platinum, and compare them with our earlier results on shock-compressed gold [11,23]. Silver and platinum, like gold, have often been used as pressure calibrants [14,16,29–31] due to their presumed structural stability, based on earlier investigations. For example, under static compression, Ag is known to be stable in its ambient fcc structure up to 150 GPa [14]. Hugoniot results also suggest the stability of the fcc structure up to $\sim$210 GPa [20–22]. Consistent with these observations, first principles stability calculations along the 0 K isotherm predict that Ag will undergo structural transformations only at much higher pressures: fcc-to-hcp transformation at $\sim$540 GPa and hcp-to-bcc transformation at $\sim$1400 GPa [32]. The high pressure—high temperature phase diagram of Ag remains theoretically unexplored. For Pt, experiments support the stability of the ambient fcc structure up to 330 GPa under static pressure [29] and to 660 GPa under shock compression [18].

In situ XRD experiments on Ag and Pt were conducted at the laser-shock experimental station of the Dynamic Compression Sector located at the Advanced Photon Source. The experimental configuration, shown in Fig. 1, is similar to that used in Refs. [11,23]. A 100 J laser having a 5 or 10 ns pulse duration was used to ablate an aluminized Kapton film, resulting in a shock wave in the Kapton which propagated into a nominally 12.5(7.5) $\mu$m thick silver (platinum) foil. Different laser pulse shapes and energies were used to generate flat-top shocked states in the foil samples with stresses ranging from 33–221 GPa for Ag and from 46–383 GPa for Pt. Shock stresses were determined from velocity interferometry measurements that recorded the velocity histories at the Ag/LiF and Pt/LiF window interfaces (see Figs. S1 and S2 [33]). Stresses and results for 24 Ag experiments and 20 Pt experiments are presented in Tables S1 and S2 of the Supplemental Material [33]. Additional details regarding the laser-shock experiments are provided in the Refs. [33,37].

The XRD measurements represent a single snapshot obtained using a $\sim$100 ps duration x-ray pulse with a bandwidth of a few percent and maximum x-ray flux at $\sim$23.5 keV (see Fig. S3 [33]). During each experiment, the crystal structure of the shocked sample was probed by recording a two-dimensional XRD image on an area
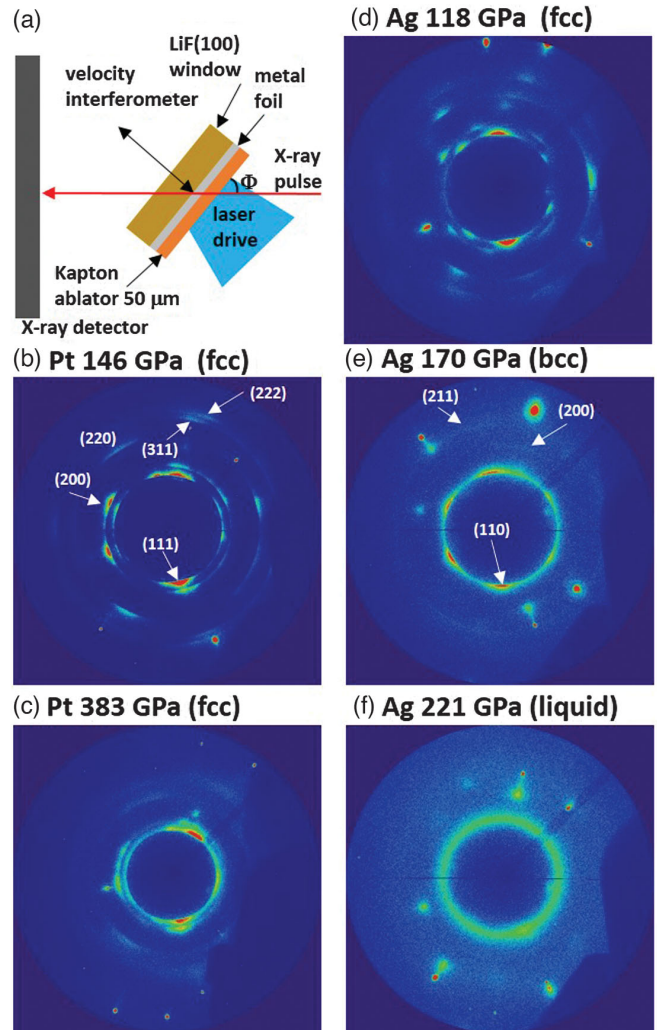


FIG. 1. (a) Schematic of the experimental configuration. (b)–(f) Representative XRD results for shocked Pt and Ag. Pt shocked to 146 and 383 GPa remains in the fcc structure. Ag shocked to 118 GPa remains fcc. Ag shocked to 170 GPa has the bcc structure and Ag shocked to 221 GPa shows a broad liquid scattering ring. The localized spots are from the single crystal LiF window.

detector while the shock wave was propagating through the sample. For all experiments below the shock melting stress, the XRD image was recorded before the shock wave reflected from the LiF window and before the release wave from the ablator entered the samples. Thus, the XRD measurements of the crystalline state contain diffraction contributions from two different states of the material: the ambient (unshocked) state and the peak shocked state.

Measured powder XRD patterns (e.g., see Fig. 1 and Fig. S4 in the Supplemental Material [33]) were converted to one-dimensional line profiles of intensity versus scattering angle ($2\theta$) by integrating around the rings using Fit2d [38]. Because these line profiles have contributions from both shocked and unshocked regions of the samples, a fraction of the ambient XRD line profile (measured for each sample just

prior to shock compression) was subtracted to obtain the XRD line profile from the shocked portion of the foil sample, as described in Ref. [11]. Representative XRD line profiles for shocked Ag and Pt are shown in Fig. 2.

To identify structural modifications (volume changes, structural transformations and/or stacking fault generation) under shock compression, the experimental XRD line profiles were quantitatively compared with simulated line profiles. The simulated profiles were computed by incorporating all the experimental parameters, such as sample thickness, angle of incidence $\Phi$ of the x-ray beam with
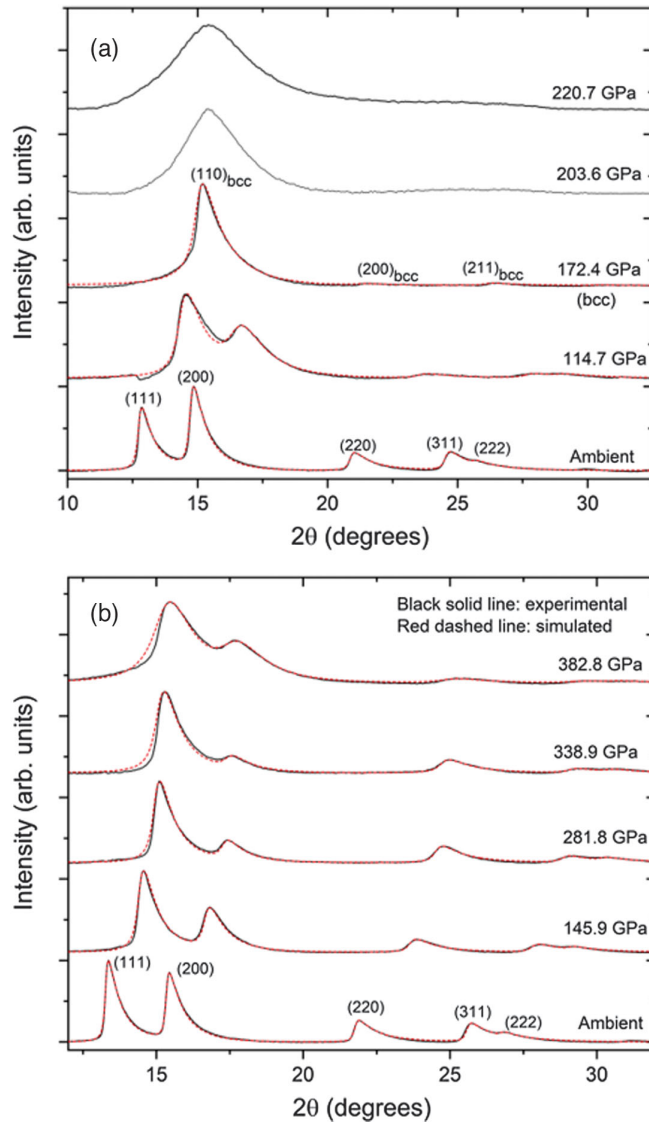


FIG. 2.   (a) Experimental and simulated line profiles for silver at several representative stresses. Only a single broad peak is observed at 203.6 and 220.7 GPa [no observable $(200)_{bcc}$ or $(211)_{bcc}$ peaks] indicating the molten phase, but the noticeably more pointed hump at 203.6 GPa possibly indicates that shock melting is not completed by 203.6 GPa. (b) Experimental and simulated line profiles for platinum at several representative stresses.

respect to the sample plane, spectral flux of x rays incident on the sample, x-ray absorption, and instrumental broadening. The effects of SFs on line profiles were incorporated in the simulations using the formalism proposed by Warren [39] and generalized by Velterop *et al.* [40]. The primary effect of SFs is to shift the (200) diffraction peak towards the (111) diffraction peak such that the application of Bragg's law will give different apparent lattice spacings for (111) and (200) diffraction peaks when SFs are present in an fcc material [39,40]. To account for texture effects on the diffraction peak intensities, the relative intensities of different simulated {hkl} peaks were varied when fitting simulations to measured line profiles. Simulated diffraction profiles were also convoluted with a Lorentzian broadening function to match the observed peak widths that increase with shock stress. A detailed description of the forward XRD simulations that incorporate SFs is presented in Ref. [11].

Figure 2(a) shows measured XRD line profiles for Ag, along with simulated XRD line profiles incorporating SFs in the fcc structure (for comparison, simulations with and without SFs are shown in Fig. S5 of the Supplemental Material [33]). Up to ∼144 GPa, the observed variations in the line profiles can be ascribed to a combination of volume compression and SF generation. The abundance of SFs, shown in Fig. 3, increases to ∼16.5% at 144.4 GPa, comparable to shock-compressed gold at ∼150 GPa [11]. The observed variation in SF abundance with volume compression is qualitatively similar to the experimental gold results [11] and the molecular dynamics (MD) simulation results [41] (see Fig. S6 [33]).

At 158.8 GPa, the line profile for Ag shows two new diffraction peaks at $2\theta \sim 21.6°$ and $26.5°$, in addition to the fcc peaks, which are indexed as {200} and {211} bcc peaks (see Fig. S7 [33]). The {110} bcc peak overlaps the {111} and {200} fcc peaks. Beyond ∼170 GPa, only bcc peaks are observed. From the width of the {110} bcc peaks, the coherently diffracting domain size is estimated to be ∼10 nm at ∼170 GPa. Above 196.8 GPa, the crystalline diffraction peaks are replaced by a significantly broader diffraction peak at $2\theta \sim 15.4°$, indicating the molten phase. Figure 4(a) shows that the peak longitudinal stress $(P_x)$-volume $(V)$ states determined from the present Ag experiments are in good agreement with the previously reported Hugoniot data [21,22,33], which have also been shown to be consistent with theoretical Hugoniot curves calculated assuming the fcc structure [43,44]. Hence, our results are consistent with a small volume change associated with the fcc-bcc transition.

In contrast to Ag and Au [23,24], shocked Pt retains the fcc structure up to ∼380 GPa [see Fig. 2(b)]. The $P_x - V$ states determined from the present Pt experiments match the previously determined Hugoniot [18] [see Fig. 4(b)]. At ∼380 GPa, the FWHM of the Pt fcc peaks is substantially increased and the texture significantly reduced, suggesting
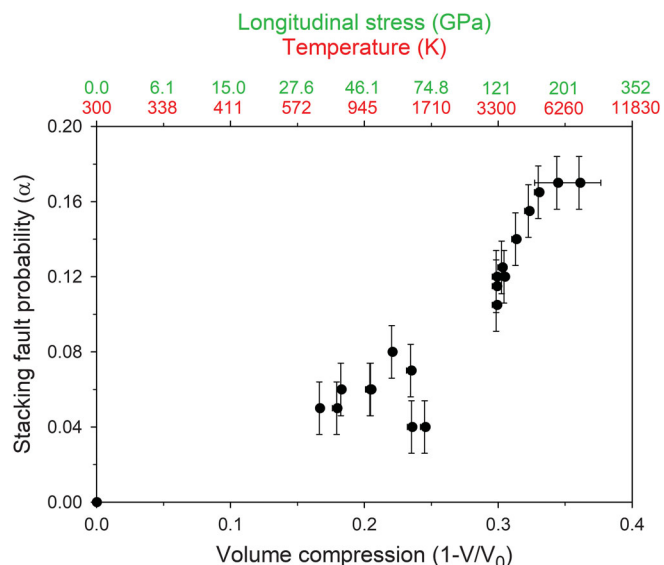
FIG. 3. Stacking fault probability versus volume compression in silver. Corresponding longitudinal stresses and calculated temperatures are shown at the top. The longitudinal stresses were determined using the reported Ag Hugoniot [21,22,33]. The calculated temperatures were determined using the silver equation of state (#2720) from the SESAME library developed at Los Alamos National Laboratory [42].

proximity to the shock melting stress. Similar features were observed recently for shocked Ge upon approaching the melt boundary [45]. Melting of shocked Pt is discussed further in the Supplemental Material [33]. The Pt diffraction patterns do not exhibit any features characteristic of SFs up to ∼339 GPa. At higher stresses, a small SF probability cannot be ruled out (∼0.02–0.06 SF probability above 349 GPa). These results indicate that shock induced deformation in platinum does not involve significant SF generation.

MD simulations suggest SF generation is a generic feature of shock compression in fcc solids [41,46,47]. However, the present results suggest strong material specificity, depending on the stacking fault energy (SFE) of the material. In particular, SFs play an important role in shock induced deformation in low SFE fcc metals (Ag and Au), but are minimally observed even at very high shock stresses (over ∼340 GPa) and volume compressions (over 30%)—approaching the melt boundary—in a high SFE fcc metal (Pt). Although the SFE may change under compression [48,49], this dependence is not known for Ag, Au, and Pt.

In contrast to the structural stability of Au and Ag under static compression (and the predicted stability of fcc Ag using first principles calculations [32]), the fcc to bcc transformation observed under shock compression shows that features unique to shock compression govern this structural change. The absence of this transformation in shocked Pt suggests that temperature increase is likely not the governing factor. As noted earlier, a distinctive feature
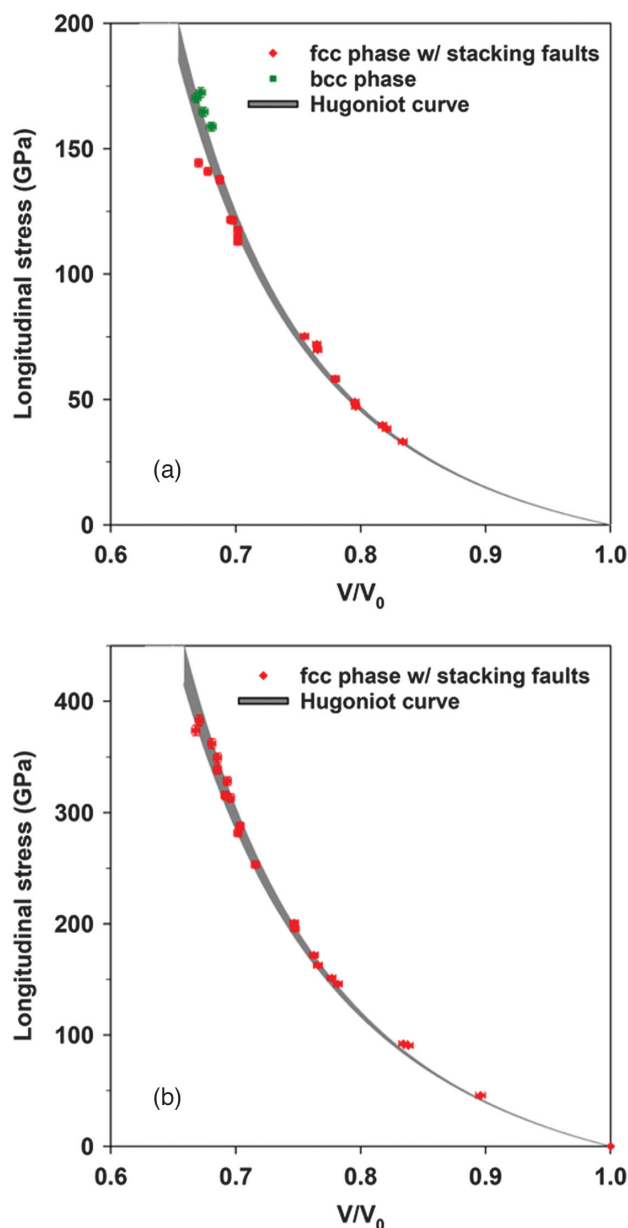


FIG. 4. (a) Comparison of $P_x - V$ states for shock compressed silver determined using XRD with the reported Ag Hugoniot [21,22,33]. (b) Comparison of $P_x - V$ states for shock compressed platinum determined using XRD with the reported Hugoniot [18,33].

of shock compression is uniaxial strain which causes plastic deformation—resulting in a high abundance of SFs in shocked Au and Ag. The fcc-bcc transformation in shocked Au and Ag at shock stresses corresponding to large SF abundance makes a strong case that SFs facilitate this transformation.

The widely studied austenite to martensite phase change in steels is a well-known rapid fcc to bcc transformation caused by lowering the temperature. Theoretical efforts to understand this transformation provide useful insights, potentially relevant to our work. Although no extant

models for this transformation are based directly on a large abundance of SFs, a hard sphere model proposed by Bogers and Burgers [50] showed that two sequential shear displacements related to Shockley partial dislocations (resulting in SFs on {111} fcc planes) can bring about the fcc to bcc transformation. Olson and Cohen [51,52] further extended this model and proposed a path through a transient hcp phase, consistent with the Kurdjumov-Sachs (KS) orientation relation [53] commonly observed in the austenite to martensite transformation. MD simulations [54] have shown that the fault band generated by the intersection of the two SFs used in the models of Bogers and Burger [50] and Olson and Cohen [51,52] becomes a preferred site for nucleation and growth of the bcc phase. Another MD simulation also supports the finding that the fcc to bcc phase change in steel evolves through the same atomic pathway [55]. Experimental studies [55] of this phase change on a plastically deformed austenite steel surface showed regions consistent with the models of Refs. [50–52], validating the role of shear displacements characteristic of Shockley partial dislocations, i.e., SFs, in facilitating this phase change. The arguments of Refs. [50–52,54,55] are broadly applicable to fcc metals having SFs, not necessarily specific to steels and iron.

To date, the effect of SFs on the fcc to bcc transformation in noble metals has not been considered in theoretical studies. Our results presented here for Ag and previously for Au [11,23] provide strong motivation—and a quantitative benchmark—for theoretical investigations regarding the role of shock-induced deformation on the fcc-bcc phase transition observed in shocked Ag and Au. It may be valuable to determine if the inclusion of SFs in the fcc phase can significantly change the predicted phase boundaries and facilitate the transformation to the bcc structure along the Hugoniot.

The experimental findings for shock compressed Ag, Au, and Pt point to two key scientific outcomes for future shock and static compression studies. The role of deformation induced microstructural changes—because they are an integral feature of shock compression—needs to be carefully considered in high pressure structural transformations. For Ag and Au, the equations of state used to determine isothermal compression curves from shock data cannot predict the fcc-bcc transformation. Hence, use of Ag and Au as a pressure calibrant above ~150 GPa is questionable because reduction of the Hugoniot curve to an isotherm presumes that the two curves differ only in temperature. Quantitative theoretical calculations are needed to determine if the free energy partitioned in defects and structural changes in these shock-compressed metals can have a significant effect on the reduced isotherm. In contrast to the results for Ag and Au, EOS studies correctly predict the fcc structure in shocked Pt, suggesting that Pt may be the most suitable element as a pressure calibrant.

---

[*]Corresponding author.
ymgupta@wsu.edu

[1] W. J. Nellis, J. A. Moriarty, A. C. Mitchell, M. Ross, R. G. Dandrea, N. W. Ashcroft, N. C. Holmes, and G. R. Gathers, Phys. Rev. Lett. **60**, 1414 (1988).

[2] H. K. Mao, P. M. Bell, J. W. Shaner, and D. J. Steinberg, J. Appl. Phys. **49**, 3276 (1978).

[3] G. E. Duvall and R. A. Graham, Rev. Mod. Phys. **49**, 523 (1977).

[4] T. d'Almeida and Y. M. Gupta, Phys. Rev. Lett. **85**, 330 (2000).

[5] D. H. Kalantar, J. F. Belak, G. W. Collins, J. D. Colvin, H. M. Davies, J. H. Eggert *et al.*, Phys. Rev. Lett. **95**, 075502 (2005).

[6] S. J. Turneaure, N. Sinclair, and Y. M. Gupta, Phys. Rev. Lett. **117**, 045502 (2016).

[7] P. Kalita, P. Specht, S. Root, N. Sinclair, A. Schuman, M. White, A. L. Cornelius, J. Smith, and S. Sinogeikin, Phys. Rev. Lett. **119**, 255701 (2017).

[8] E. E. McBride, A. Krygier, A. Ehnes, E. Galtier, M. Harmand, Z. Konopkova *et al.*, Nat. Phys. **15**, 89 (2019).

[9] C. E. Wehrenberg, D. McGonegle, C. Bolme, A. Higginbotham, A. Lazicki, H. J. Lee, B. Nagler, H.-S. Park, B. A. Remington, R. E. Rudd, M. Sliwa, M. Suggit, D. Swift, F. Tavella, L. Zepeda-Ruiz, and J. S. Wark, Nature (London) **550**, 496 (2017).

[10] S. J. Turneaure, P. Renganathan, J. M. Winey, and Y. M. Gupta, Phys. Rev. Lett. **120**, 265503 (2018).

[11] S. M. Sharma, S. J. Turneaure, J. M. Winey, P. A. Rigg, N. Sinclair, X. Wang, Y. Toyoda, and Y. M. Gupta, Phys. Rev. X **10**, 011010 (2020).

[12] D. L. Heinz and R. Jeanloz, J. Appl. Phys. **55**, 885 (1984).

[13] A. Dewaele, P. Loubeyre, and M. Mezouar, Phys. Rev. B **70**, 094112 (2004).

[14] Y. Akahama, H. Kawamura, and A. K. Singh, J. Appl. Phys. **95**, 4767 (2004).

[15] K. Takemura and A. Dewaele, Phys. Rev. B **78,** 104119 (2008).

[16] A. Dewaele, M. Torrent, P. Loubeyre, and M. Mezouar, Phys. Rev. B **78,** 104102 (2008).

[17] A. Dewaele, P. Loubeyre, F. Occelli, O. Marie, and M. Mezouar, Nat. Commun. **9,** 2913 (2018).

[18] N. C. Holmes, J. A. Moriarty, G. R. Gathers, and W. J. Nellis, J. Appl. Phys. **66,** 2962 (1989).

[19] M. Yokoo, N. Kawai, K. G. Nakamura, K. I. Kondo, Y. Tange, and T. Tsuchiya, Phys. Rev. B **80,** 104114 (2009).

[20] R. G. McQueen and S. P. Marsh, J. Appl. Phys. **31,** 1253 (1960).

[21] *LASL Shock Hugoniot Data*, edited by S. P. Marsh (University of California Press, Los Angeles, 1980), p. 131.

[22] L. V. Altshuler, A. A. Bakanova, I. P. Dudoladov, E. A. Dynin, R. F. Trunin, and B. S. Chekin, J. Appl. Mech. Tech. Phys. **22,** 145 (1981).

[23] S. M. Sharma, S. J. Turneaure, J. M. Winey, Y. Li, P. A. Rigg, A. Schuman, N. Sinclair, Y. Toyoda, X. Wang, N. Weir, J. Zhang, and Y. M. Gupta, Phys. Rev. Lett. **123,** 045702 (2019).

[24] R. Briggs, F. Coppari, M. G. Gorman, R. F. Smith, S. J. Tracy, A. L. Coleman, A. Fernandez-Pañella, M. Millot, J. H. Eggert, and D. E. Fratanduono, Phys. Rev. Lett. **123,** 045701 (2019).

[25] N. A. Smirnov, J. Phys. Condens. Matter **29,** 105402 (2017).

[26] J. P. Hirth and J. L. Lothe, *Theory of Dislocations*, 2nd ed. (Wiley, New York, 1982).

[27] P. C. J. Gallagher, Metall. Trans. **1,** 2429 (1970).

[28] R. Li, S. Lu, D. Kim, S. Schönecker, J. Zhao, S. K. Kwon, and L. Vitos, J. Phys. Condens. Matter **28,** 395001 (2016).

[29] A. K. Singh, H. P. Liermann, Y. Akahama, S. K. Saxena, and E. M. Proupin, J. Appl. Phys. **103,** 063524 (2008).

[30] M. Matsui, E. Ito, T. Katsura, D. Yamazaki, T. Yoshino, A. Yokoyama, and K. Funakoshi, J. Appl. Phys. **105,** 013505 (2009).

[31] K. Jin, Q. Wu, H. Geng, X. Li, L. Cai, and X. Zhou, High Press. Res. **31,** 560 (2011).

[32] J. C. Boettger, Int. J. Quantum Chem. **112,** 3822 (2012).

[33] See Supplemental Material at http://link.aps.org/supplemental/10.1103/PhysRevLett.124.235701 for additional details regarding the experiments and analysis, which includes Refs. [34–36].

[34] L. M. Barker and R. E. Hollenbach, J. Appl. Phys. **43,** 4669 (1972).

[35] P. A. Rigg, M. D. Knudson, R. J. Scharff, and R. S. Hixson, J. Appl. Phys. **116,** 033515 (2014).

[36] S. Anzellini, V. Monteseguro, E. Bandiello, A. Dewaele, L. Burakovsky, and D. Errandonea, Sci. Rep. **9,** 13034 (2019).

[37] X. Wang, P. Rigg, J. Sethian, N. Sinclair, N. Weir, B. Williams, J. Zhang, J. Hawreliak, Y. Toyoda, Y. M. Gupta, Y. Li, D. Broege, J. Bromage, R. Earley, D. Guy, and J. Zuegel, Rev. Sci. Instrum. **90,** 053901 (2019).

[38] A. P. Hammersley, ESRF Internal Report No. ESRF97-HA02T 1997.

[39] B. E. Warren, *X-Ray Diffraction* (Addison-Wesley, Reading, 1969).

[40] L. Velterop, R. Delhez, T. H. de Keijser, E. J. Mittemeijer, and D. Reefman, J. Appl. Crystallogr. **33,** 296 (2000).

[41] B. L. Holian and P. S. Lomdahl, Science **280,** 2085 (1998).

[42] SESAME: The Los Alamos National Laboratory Equation of State Database, edited by S. P. Lyon and J. D. Johnson, Los Alamos National Laboratory Tech. Rep. LA-UR-92-3407, 1992.

[43] I. V. Lomonosov, J. Phys. Conf. Ser. **946,** 012081 (2018).

[44] R. H. Joshi, B. Y. Thakore, N. K. Bhatt, P. R. Vyas, and A. R. Jani, Physica (Amsterdam) **530B,** 160 (2018).

[45] P. Renganathan, S. J. Turneaure, S. M. Sharma, and Y. M. Gupta, Phys. Rev. B **99,** 134101 (2019).

[46] T. C. Germann, B. L. Holian, P. S. Lomdahl, and R. Ravelo, Phys. Rev. Lett. **84,** 5351 (2000).

[47] T. C. Germann, D. Tanguy, B. L. Holian, P. S. Lomdahl, M. Mareschal, and R. Ravelo, Metall. Mater. Trans. A **35,** 2609 (2004).

[48] P. Andric, B. Yin, and W. A. Curtin, J. Mech. Phys. Solids **122,** 262 (2019).

[49] P. S. Branicio, J. Y. Zhang, and D. J. Srolovitz, Phys. Rev. B **88,** 064104 (2013).

[50] A. J. Bogers and W. G. Burgers, Acta Metall. **12,** 255 (1964).

[51] G. B. Olson and M. Cohen, Metall. Trans. A **7,** 1905 (1976).

[52] G. B. Olson and M. Cohen, Annu. Rev. Mater. Sci. **11,** 1 (1981).

[53] G. V. Kurdjumov and G. Sachs, Z. Phys. **64,** 325 (1930).

[54] C. W. Sinclair and R. G. Hoagland, Acta Mater. **56,** 4160 (2008).

[55] X. S. Yang, S. Sun, X. L. Wu, E. Ma, and T. Y. Zhang, Sci. Rep. **4,** 6141 (2014).